Supplementary Information
Topological structure and dynamics of three-dimensional active nematics

Guillaume Duclos[1,#], Raymond Adkins[2,#], Debarghya Banerjee[3,4], Matthew S. E. Peterson[1], Minu Varghese[1], Itamar Kolvin[2], Arvind Baskaran[1], Robert A. Pelcovits[5], Thomas R. Powers[5,6], Aparna Baskaran[1], Federico Toschi[7], Michael F. Hagan[1], Sebastian J. Streichan[2], Vincenzo Vitelli[8], Daniel A. Beller[9,*], and Zvonimir Dogic[1,2,*]

[1]*Department of Physics, Brandeis University, 415 South Street, Waltham, Massachusetts 02453, USA*
[2]*Department of Physics, University of California, Santa Barbara, California 93111, USA*
[3]*Max Planck Institute for Dynamics and Self-Organization, Am Faßberg 17, 37077 Göttingen, Germany*
[4]*Instituut-Lorentz, Universiteit Leiden, 2300 RA Leiden, Netherlands*
[5]*Department of Physics, Brown University, Providence, Rhode Island 02912, USA*
[6]*School of Engineering, Brown University, Providence, Rhode Island 02912, USA*
[7]*Department of Applied Physics, Eindhoven University of Technology, 5600 MB Eindhoven, Netherlands*
[8]*James Frank Institute and Department of Physics, The University of Chicago, Chicago, Illinois 60637, USA*
[9]*Department of Physics, University of California, Merced, California 95343, USA*
[#]*These authors contributed equally to the manuscript*
[*]*Correspondence to: dbeller@ucmerced.edu, zdogic@ucsb.edu*

1 Experimental methods

Microtubule polymerization: Tubulin dimers were purified from bovine brains, through two cycles of polymerizations and depolymerizations in a high molarity PIPES buffer (*1*). Tubulin was flash frozen and stored at -80 °C in M2B buffer (80 mM PIPES, pH 6.8, 1 mM EGTA, 2 mM $MgCl_2$). Tubulin was labeled with Alexa-Fluor 647-NHS (Invitrogen, A-20006) as previously described (*2*). To induce polymerization, tubulin (80 μM in M2B) was mixed with 0.6mM GMCPP (Jena Biosciences, NU-4056) and 1mM dithiothreitol DTT in M2B. 3% of the tubulin was fluorescently labeled. The tubulin was first incubated for 30 min at 37°C, followed by an annealing step at room temperature for 6 hours. The GMPCPP stabilized microtubules have an average length of 1.5 μm (*3*). The polymerized microtubules were then flash frozen and stored at -80°C.

Assembly of kinesin clusters: K401-BIO-6xHIS is the 401 amino acid N-terminal domain derived from the Drosophila melanogaster kinesin-1 and labeled with a 6-his and a biotin tag. The motor proteins were transformed, expressed in Rosetta (DE3) pLysS *E. coli* cells, and purified as described previously (*4*). The purified proteins were flash frozen in liquid nitrogen with 36% sucrose and stored at -80 °C. The K401 biotin-labeled motors were assembled into multimotor clusters using tetravalent streptavidin (ThermoFisher, 21122). We mixed 5 μL of 6.4 μM kinesin motors with 5.7 μL of 6.6 μM streptavidin (MW: 52.8 kDa) in 1.7:1 biotin to streptavidin ratio, and 0.5 μL of 5 mM dithiothreitol (DTT) in M2B (80 mM PIPES,pH 6.8, 1 mM EGTA, 2 mM $MgCl_2$). The clusters were then incubated on ice for 30 min, before being flash frozen and stored at -80C.

PRC-1 purification: The truncated PRC1-NSΔC (MW: 58 kDa) was used to specifically crosslink microtubules while still allowing for their sliding. It consists of the first 486 amino acids of the full length PRC1 protein (MW: 72.5 kDa). The protein was transformed and expressed in Rosetta BL21(DE3) cells,

and subsequently purified as described previously (*5*). The truncated form of PRC1 has greatly increased stability, while maintaining the dimerization and the microtubule binding domaina and allowing for assembly of active fluids that exhibit chaotic flows (*6*).

Colloidal virus purification: Filamentous virus fd-wt and fd-Y21M were purified andn characterized as described previously (*7*, *8*). All samples were stored in high salt 20 mM Tris buffer (pH 8.0, 100 mM NaCl). fd-Y21M forms a colloidal nematic liquid crystal phases as predicted by the Onsager theory of hard rods (*8*)

Assembling active nematic liquid crystal: We assembled active nematics by doping an *fd* colloidal liquid crystal with extensile microtubule bundles. A pre-mixture was prepared in a high salt M2B (M2B + 3.9 mM $MgCl_2$) containing an oxygen scavenging system (3.3 mg/mL glucose, DTT (5.5 mM), glucose oxidase (Sigma, G2133) and catalase (0.038 mg/mL, Sigma, C40)), 2nM Trolox to reduce photobleaching (Sigma, 238813), ATP (1420 uM), an ATP regeneration system (phosphoenol pyruvate (26 mM PEP, Beantown Chemical, 129745) and pyruvate kinase/lactate dehydrogenase enzymes (2.8% v/v PK/LDH, Sigma, P-0294)). We then added the kinesin clusters (121 nM Streptavidin), PRC-1 (200nM), *fd* viruses (25 mg/mL) and microtubules (13 μM). Typical samples consist of 7 mL of Premix, 3 mL of fd virus (100 mg/mL) and 2mL of microtubules (8 mg/mL). The samples are typically active for 3 hours. Passive samples were assembled using the same recipe but lacked both ATP and the kinesin clusters. The isotropic samples were obtained by assembling the previous recipe without fd-wt viruses. For SPIM imaging, the ATP concentration was reduced to 100 μM. The acquisition time (12 sec) of a 3D stack was small compared to the typical fluid velocity, which is less than 0.1 μm/sec.

Widefield microscopy: Samples were imaged with an inverted microscope (Nikon Ti-E) equipped with a XYZ motorized stage, polarization optics, and a fluorescence imaging module. Simultaneous pictures of the birefringence and the fluorescent microtubules were obtained with a 20x objective (Pan Fluor, NA 0.75) and a CCD camera (Andor, Clara E).

Multiview-SPIM imaging: The 3D samples were imaged using multi-view light sheet microscopy (*9*). Briefly, the microscope is composed of two detection and illumination arms. The detection arm is an epifluorescence microscope, consisting of a water-dipping objective (Apo LWD 25x, NA 1.1, Nikon Instruments Inc.), a filter wheel (HS-1032, Finger Lakes Instrumentation LLC), emission filters (BLP01-488R-25, BLP02-561R-25, Semrock Inc.), a tube lens (200 mm, Nikon Instruments Inc.), and an sCMOS camera (ORCA-Flash4.0 V3 Digital) with an effective pixel size of 0.26 μm. The illumination arm consisted of a water-dipping objective (CFI Plan Fluor 10x, NA 0.3), a tube lens (200 mm, both Nikon Instruments Inc.), a scan lens (S4LFT0061/065, Sill optics GmbH and Co. KG), a galvanometric scanner (6215 hr, Cambridge Technology Inc.), and two lasers (06-MLD 488 nm, Cobolt AB, and 660LX/LS OBIS 660 nm, Coherent Inc.). The FEP tubing is translated using a linear piezo stage (P-629.1cd with E-753 controller) and rotated using a rotational piezo stage (U-628.03 with C-867 controller) and a linear actuator (M-231.17 with C-863 controller, all Physik Instrumente GmbH and Co. KG). Samples were recorded using 4 views, by 900 rotated views, 200 slices with an optical sectioning of 2 μm, and a temporal resolution of either 12 or 20s depending if tracer beads were also imaged. Sample were mounted in a FEP tube of 800 μm inner diameter and sealed with NOA UV glue. The immersion water for the objectives was suplemented with 7.4% sucrose to mach the refractive index of the FEP tubing (n=1.344).

Image post-processing: data fusion and deconvolution: Image processing was performed using Matlab, Fiji and associated multi-view deconvolution plugin (*10*, *11*). The light sheet data was unpacked and binned (2*2 binning, spatial resolution of 0.52 μm after binning) using a custom made Matlab program. To ensure a correct measurement of the microtubule orientation, we first removed distortions introduced by an anisotropic point-spread function (PSF) - SPIM being subject to optical aberration. We deconvolved the four views post-acquisition using an empirical PSF measured on passive fluorescent particles immersed in the active LC (20 iterations). Finally, the same markers were used to register the four complementary views of sample taken at 90 deg rotation intervals, which also reduced the effect of the anisotropic PSF.

3D Orientation analysis: The 3D nematic director field was extracted by computing the local structure tensor in 3D with a custom-made Matlab code. This method has been described previously for 2D sam-

ples (*12*). The Gaussian window size was ≈6 μm. Choosing the right window size is important for corect detection of the topological defects. Choosing a smaller window size resulted in false positives. Choosing a larger window size led to smoothing of the nematic director, and increased the number of undetected defects. To find the defects, we first computed the distortion energy in the one-elastic constant approximation, approximating spatial partial derivatives ∂_i with finite differences. We did not measure $(\partial_i n_j)(\partial_i n_j)$. Instead we measured $(\partial_i[n_j n_k])(\partial_i[n_j n_k])$. In principle these two provide the same information. However, the first option picks up a large artificial derivative when n flips to -n, and then squares that derivative. The second option fixes the n = -n problem by taking derivatives of $n_j n_k$ instead of just n_j, removing the large artificial derivatives. We then looked at the winding of the director field where the distortion energy was greater than a 0.5 threshold. We verified that the defects' detection did not depend on the energy treshold chosen. We manually verified that the defects observed in the nematic field correspond to disclinations in the fluorescent microtubule channel. We found that about 20% of the detected defects were false positives, principally due to a low signal/noise ratio in regions where the light sheet is not in focus (on the edge of the FOV).

2 Numerical methods

Theoretical model: The state of an active nematic is defined by a flow velocity field **u** and a tensor order parameter field Q_{ij} that gives the orientation of the nematics in the flow. The evolution of these two fields is modeled with the Beris-Edwards equations with an added active stress term: the flow field evolves according to the Navier-Stokes equation with additional stress terms due to the nematic order and activity. Meanwhile, Q_{ij} evolves in the flow by advection and free energy relaxation. We can write the equations for active nematics (*13*) as:

$$\left(\partial_t + u_k\partial_k\right) Q_{ij} - S_{ij} = \Gamma H_{ij}, \tag{1}$$

$$\rho\left(\partial_t + u_k\partial_k\right) u_i = \partial_j \Pi_{ij}. \tag{2}$$

$$\partial_i u_i = 0. \tag{3}$$

Here, ρ is the density (assumed constant), Γ is a rotational diffusion constant, Π_{ij} is the total stress tensor, and S_{ij} is the generalized advection term:

$$S_{ij} = \left(\xi E_{ik} + \Omega_{ik}\right)\left(Q_{kj} + \delta_{kj}/3\right) + \left(Q_{ik} + \delta_{ik}/3\right)\left(\xi E_{kj} - \Omega_{kj}\right) - 2\xi\left(Q_{ij} + \delta_{ij}/3\right)\left(Q_{kl}\partial_k u_l\right). \tag{4}$$

In this expression, ξ is a constant determining flow-aligning or tumbling behavior, and the symmetric and the anti-symmetric spatial derivatives of the velocity field are:

$$E_{ij} = \frac{1}{2}\left(\partial_j u_i + \partial_i u_j\right),$$

$$\Omega_{ij} = \frac{1}{2}\left(\partial_j u_i - \partial_i u_j\right).$$

The relaxation due to the free energy is given by the molecular field H_{ij}, which is defined as:

$$H_{ij} = -\delta\mathcal{F}/\delta Q_{ij} + (\delta_{ij}/3)\mathrm{Tr}(\delta\mathcal{F}/\delta Q_{kl}), \tag{5}$$

$$\mathcal{F} = K(\partial_k Q_{ij})^2/2 + AQ_{ij}Q_{ji}/2 + BQ_{ij}Q_{jk}Q_{ki}/3 + C(Q_{ij}Q_{ji})^2/4. \tag{6}$$

In the free energy, K is the single Frank elastic constant, and the Landau expansion coefficients A, B, C control the isotropic-nematic phase transition.

The stress tensor Π_{ij} consists of a sum of the viscous stress, the passive stress, and the active stress. The active stress is given by $\Pi^a_{ij} = -\zeta Q_{ij}$, where the activity parameter ζ is positive for extensile systems and negative for contractile systems. The passive stress is

$$\begin{aligned}\Pi^p_{ij} \;=\; & -p\delta_{ij} + 2\xi(Q_{ij} + \delta_{ij}/3)(Q_{kl}H_{lk}) \\ & -\xi H_{ik}(Q_{kj} + \delta_{kj}/3) - \xi(Q_{ik} + \delta_{ik}/3)H_{kj} \\ & -\partial_i Q_{kl}(\delta\mathcal{F}/\delta\partial_j Q_{lk}) + Q_{ik}H_{kj} - H_{ik}Q_{kj},\end{aligned}$$

The viscous stress given by $\Pi_{ij}^{\rm vis} = 2\mu E_{ij}$.

Hybrid lattice Boltzmann method: We solve the above set of equations using a hybrid lattice Boltzmann method in the limit of high viscosity (to ensure low Reynolds number) (*13*). The hybrid lattice Boltzmann method employs a lattice Boltzmann method to evolve $\mathbf{u}$ according to the (modified) Navier-Stokes equation and a finite difference method to calculate the evolution equation of the Q–tensor. The feedback of the Q–tensor field enters the Navier-Stokes equation as a forcing term. The time integration of the Q–tensor field is done using a second order Adams-Bashforth method. The parameters used for the simulations are $\Gamma = 0.33$, $\mu = 0.67$, $\xi = 0.9$, $K = 0.005$, $\zeta = 0.01$, $-B = C = 0.1$, and $A = 0$. Incompressibility ($\partial_j u_j = 0$) of the flow is ensured by keeping the Mach number sufficiently low.

Zero Reynolds number limit: Finite difference Stokes solver method: The phenomenology observed in the experiments described here can be predicted from a minimal model for active nematics where the flows are quasi-static and purely due to viscous and active stresses. To demonstrate this, we consider Equation 1 with terms up to second order in the dynamic variables, coupled to an incompressible Stokes flow driven entirely by viscous and active stresses. Non-dimensionalizing the equations gives the following dimensionless parameters: $K^* = \Gamma t_0 K/l_0^2$, $\mu^* = \frac{\mu t_0 l_0}{m_0}$, $\zeta^* = \frac{\zeta l_0 t_0^2}{m_0}$ $A^* = \Gamma t_0 A$, $B^* = \Gamma t_0 B$, $C^* = \Gamma t_0 C$. We chose $K^* = 1$, $\mu^* = 1$, $\zeta^* = 0.2$ and $A^* = -1/3, B^* = -4, C^* = 4$ so that our simulation units are given by $t_0 = 4/(\Gamma C)$, $l_0 = 2\sqrt{K/C}$, $m_0 = 8\mu\sqrt{K}/(\Gamma\sqrt{C^3})$. To ensure numerical stability while solving Equation 1, we use a semi-implicit finite difference time stepping scheme based on a convex splitting of the nematic free energy (*14*). To solve the Stokes equation and enforce incompressibility, we implement a Vanka type box smoothing algorithm on a staggered grid (*15*). The solution at each time step is found using Gauss Seidel relaxation iterations, and the rate of convergence to the solution is accelerated by our multigrid solver.

3 Theoretical calculations

Rotation vector: The rotation vector $\mathbf{\Omega}$ used in this work is the rotation angle specifying the symmetry operation in order parameter space, $\mathbb{R}P^2$, undergone by the director $\mathbf{n}(\mathbf{x})$, on a small closed measuring circuit C around the disclination at the point of interest (*16*). For all disclinations studied in this work, the angle of rotation is $|\mathbf{\Omega}| = \pi$, which corresponds to topological winding numbers of $\pm$ 1/2. The axis of rotation, $\hat{\mathbf{\Omega}} \equiv \mathbf{\Omega}/|\mathbf{\Omega}|$, is determined from the closed loop Γ in $\mathbb{R}P^2$ traced out by $\mathbf{n}$ on the measuring circuit C. Because Γ is, in general, approximately a semi-great circle, $\hat{\mathbf{\Omega}}$ is simply the normal to the semi-circle, with sign given by the positive sense of rotation on Γ as C is traversed in the positive sense (Fig. 2D). Near the defect point of interest, $\mathbf{n}$ is (approximately) confined to the plane orthogonal to $\mathbf{\Omega}$. We can form an orthonormal triad $\{\mathbf{n}_0, \mathbf{n}_1, \hat{\mathbf{\Omega}}\}$ such that, along C, $\mathbf{n}$ rotates from $\mathbf{n}_0$ through $\mathbf{n}_1$ into $-\mathbf{n}_0$.

Topological classification of disclination loops: The classification of topological defects in this work follows the standard application of homotopy theory to nematics. Disclination loops, like hedgehog point defects, carry an integer hedgehog charge:

$$d = \frac{1}{4\pi}\int_{\mathbb{S}^2} d\theta d\phi\, \mathbf{n}\cdot[\partial_\theta \mathbf{n}\times\partial_\phi \mathbf{n}], \tag{7}$$

identifying the defect with an element of the second homotopy group $\pi_2(\mathbb{R}P^2) \cong \mathbb{Z}$ (*17*). Whereas hedgehogs with different d are topologically distinct, for disclination loops the topological categorization depends only on d modulo 2 (*17*). We refer to loops with even d as topologically neutral, because shrinking a $d = 0$ loop to a point leaves behind a locally defect-free director field.

The topological information about a disclination loop is obtained using a meauring torus $\mathbb{T}^2$ enclosing the defect. Maps from $\mathbb{R}P^2$ to $\mathbb{T}^2$ are divided into four topologically distinct classes with a $\mathbb{Z}_4$ group structure when joining loops together (*18*). We classify a disclination loop's topology by recording $\mathbf{\Omega}$ and $\mathbf{n}_{\rm out}$, which together specify the disclination profile, at several sampled points along the disclination's length. The choice of $\mathbf{n}_{\rm out}$ as reference director follows the canonical choice of tracking $\mathbf{n}$ along a cycle of the torus unlinked

with the disclination (*18*). Together, $\{\mathbf{n}_{\text{out}}, \mathbf{n}_{\text{in}}, \hat{\mathbf{\Omega}}\}$ define an orthonormal frame $\mathbf{F}$, where $\mathbf{n}_{\text{in}} \equiv \hat{\mathbf{\Omega}} \times \mathbf{n}_{\text{out}}$ is the director on the inner side of the loop. Importantly, $\tilde{\mathbf{F}} \equiv \{-\mathbf{n}_{\text{out}}, -\mathbf{n}_{\text{in}}, \hat{\mathbf{\Omega}}\}$ gives the same profile as $\mathbf{F}$ because of the $\mathbf{n} \equiv -\mathbf{n}$ symmetry of the director. From point to point on a disclination loop parametrized by angle θ, the frame $\mathbf{F}$ rotates according to $\mathbf{F}(\theta_{i+1}) = \mathbf{R}_{i,i+1}\mathbf{F}(\theta_i)$, where $\mathbf{R}$ is an element of the group $SO(3)$ of rotations of a 3D rigid body. Upon traversing the loop completely, $\mathbf{F}(\theta = 2\pi)$ must return to either $\mathbf{F}(\theta = 0)$ or $\tilde{\mathbf{F}}(\theta = 0)$. In the latter case, the disclination loop is linked by another disclination loop (or an odd number of them), a situation that we do not observe in experimental or simulated active nematics. If $\mathbf{F}$ returns to itself, then the loop is unlinked, and falls into the even-d or the odd-d class.

Let Υ be the path in $SO(3)$ representing the composition of all the rotations between N sampled points, $\mathbf{R}_{0,2\pi} = \mathbf{R}_{0,\theta_1}\mathbf{R}_{\theta_1,\theta_2}\cdots\mathbf{R}_{\theta_{N-1},2\pi}$. To topologically classify these paths, we lift Υ from $SO(3)$ to the simply connected covering space $SU(2)$, which can be parametrized by the unit quaternions ($\pm i$, $\pm j$, $\pm k$, ± 1, and their multiplicative products). Following the spirit of Ref. (*19*), we choose a parametrization in which $\pm k$ represent the rotation of $\mathbf{n}_{\text{out}}$ by π about $\pm\mathbf{\Omega}$. The set of all possible total rotations $\mathbf{R}_{0,2\pi}$ is then represented by $\{1, k, -1, -k\} = k^\nu$, $\nu \in \{0, 1, 2, 3\}$ (*18*, *19*), forming a group under multiplication with the requisite $\mathbb{Z}_4$ structure. The mod-4 integer ν provides a topological index for the loop: topologically neutral loops have $\nu = 0$, topologically charged loops have $\nu = 2$, and the linked-loop scenario corresponds to $\nu = 1$ or 3. Disclination loops with approximately uniform $\mathbf{\Omega}$ and $\mathbf{n}_{\text{out}}$, which are the focus of this work, are trivially $\nu = 0$ loops, and therefore neutral and unlinked. The practical application of this theory, to calculate ν in observed disclination loops, is described below in Sec. 4.

A local formula for β, the angle between rotation vector $\mathbf{\Omega}$ and unit tangent $\mathbf{t}$: Experimental and simulated defect sets presented in this work are color-coded by β. The tangent vector is calculated straightforwardly from the separation between neighboring points on the disclination contour. We compute $\mathbf{\Omega}$ and thus β from $\mathbf{n}$ in a circuit around the loop of interest as described in Sec. 4. The small measuring circuit makes this calculation non-local in a mild way, which is feasible for individual loops but less practical for datasets of many defects.

We also used an alternative, purely local calculation of $\mathbf{\Omega}$ that agrees well with the non-local calculation: The direction of $\mathbf{\Omega}$ is estimated to be parallel to:

$$\tilde{\mathbf{\Omega}} \equiv \nabla \times \mathbf{n} - \mathbf{n}(\mathbf{n} \cdot \nabla \times \mathbf{n}) = \mathbf{n} \times [(\mathbf{n} \cdot \nabla)\mathbf{n}] \tag{8}$$

whereever $\tilde{\mathbf{\Omega}}$ has nonzero magnitude. The assumption $\mathbf{\Omega} \parallel \tilde{\mathbf{\Omega}}$ can be justified since they are exactly parallel for a straight disclination along the z-axis with uniform $\mathbf{\Omega}$, and with an idealized director field profile given by

$$\mathbf{n} = \hat{p}_1 \cos(\phi/2) + \hat{p}_2 \sin(\phi/2) \tag{9}$$

which produces a π winding of $\mathbf{n}$ about an arbitrary $\tilde{\mathbf{\Omega}}$. Here, ϕ is the angle in the xy plane, and $\{\hat{p}_1, \hat{p}_2, \hat{\mathbf{\Omega}}\}$ is an orthonormal triad. We therefore expect $\tilde{\mathbf{\Omega}}$ to be a good approximation to the direction of $\mathbf{\Omega}$ except where the disclination is strongly curved, has a rapidly varying $\mathbf{\Omega}$, or has $\beta = \pi/2$ exactly (in which case $\tilde{\mathbf{\Omega}}$ has zero length). In contrast to the non-local measurement of $\mathbf{\Omega}$ on a circuit, $\tilde{\mathbf{\Omega}}$ is a local measurement depending only on neighboring voxels for finite difference calculations of first derivatives of $\mathbf{n}$.

A separate measure is needed to choose between $\tilde{\mathbf{\Omega}}$ and $-\tilde{\mathbf{\Omega}}$ for the direction of $\mathbf{\Omega}$, because Eq. 8 is odd in $\mathbf{n}$. We use the saddle-splay energy density expression:

$$\tilde{f}_{24} \equiv \nabla \cdot [(\mathbf{n} \cdot \nabla)\mathbf{n} - \mathbf{n}(\nabla \cdot \mathbf{n})]. \tag{10}$$

Applying this expression to the ideal disclination director field of Eq. 9 shows that $\tilde{f}_{24}$ is positive at a $+1/2$ wedge profile, negative at a $-1/2$ wedge profile, and zero at a twist profile (*20*). We find that $\tilde{f}_{24}$ alone is not a reliable measure of β in the data, but that we can use the sign of $\tilde{f}_{24}$ to fix the sign of $\tilde{\mathbf{\Omega}}$ relative to the tangent. With this combination of $\tilde{\mathbf{\Omega}}$ and $\tilde{f}_{24}$, we obtain an estimate of the direction of $\mathbf{\Omega}$ with the correct sign of $\mathbf{\Omega} \cdot \mathbf{t}$, from which we obtain the angle β.

4 Data analysis

Identifying defect loops in director fields: We identify the defect set in a voxelated director field as the set of all voxels where the magnitude of the gradient in the director, $|\nabla \mathbf{n}| = \sqrt{\partial_i n_j \partial_i n_j}$, exceeds a threshold, typically 0.5–0.6. The defect set is divided into its connected subsets, each of which is a defect. To differentiate loops from other defect structures, we filter these connected subsets by their topological genus. The genus, g, which counts the number of holes, can be computed from the Euler characteristic, χ, through the relation $\chi = 2 - 2g$. Because a connected subset is a collection of cubic voxels, we can treat the subset as a polyhedron. Then, we can compute the Euler characteristic as

$$\chi = V - E + F, \tag{11}$$

where V, E, and F are the number of vertices, edges, and faces of the polyhedron, respectively.

A connected subset $\mathcal{D}$ is a collection of cubic voxels which has an easily counted number of vertices, edges, and faces, from which we calculate the Euler characteristic. To avoid spurious one-voxel holes, we inflate $\mathcal{D}$ by adding to it all of the nearest-neighbor voxels to each of the original voxels of $\mathcal{D}$ (without repetition). The computation of the Euler characteristic can be sped up using pre-computed information about possible voxel cluster motifs (*21*, *22*). From the Euler characteristic we obtain the genus and identify loops as connected subsets with $g = 1$.

Calculating a loop core: Once a connected defect subset $\mathcal{D}$ has been identified as a loop, we obtain the director profiles and calculate $\mathbf{\Omega}$ at several points on the loop. We first identify a loop core, a one-voxel-thick thread through the disclination contour, to guarantee a nontrivial winding of the director field in a small circuit around the disclination. Our algorithm to compute the defect loop core $\mathcal{C}$ chooses a starting point $\mathbf{x}_{\text{start}}$ as the location of the smallest value of nematic order S (simulation) or the largest value of $|\nabla \mathbf{n}|$ (experiment) in the connected subset. Then, successive points in the loop core are chosen as follows:

1. Construct a list $\{\mathbf{x}_i\}_{\text{elig.}}$ of eligible next points in $\mathcal{C}$, choosing from among the nearest-neighbor points to the most recently added point $\mathbf{x}_{\text{prev}}$ in $\mathcal{C}$, and selecting only those neighbors that are members of $\mathcal{D}$ but not already members of $\mathcal{C}$. Exclude any points that are in the list $\{\mathbf{x}_i\}_{\text{excl.}}$ of excluded points (defined below). Further specify that $\{\mathbf{x}_i\}_{\text{elig.}}$ cannot include any point that is a nearest neighbor of any point already in $\mathcal{C}$ besides $\mathbf{x}_{\text{prev}}$ and $\mathbf{x}_{\text{start}}$, unless this requirement leaves zero eligible next points in $\{\mathbf{x}_i\}_{\text{elig.}}$.

2. If $\mathbf{x}_{\text{prev}}$ is not a nearest neighbor of $\mathbf{x}_{\text{start}}$, but at least one of the eligible next points in $\{\mathbf{x}_i\}_{\text{elig.}}$ *is* a nearest neighbor of $\mathbf{x}_{\text{start}}$, then choose one of those points neighboring $\mathbf{x}_{\text{start}}$ as the next point $\mathbf{x}_{\text{next}}$ in $\mathcal{C}$ in order to close the loop. Otherwise, choose the next point $\mathbf{x}_{\text{next}}$ according to smallest S or largest $|\nabla \mathbf{n}|$ among the options in $\{\mathbf{x}_i\}_{\text{elig.}}$. Append $\mathbf{x}_{\text{next}}$ to $\mathcal{C}$. If this operation is not possible because there are no eligible next points in $\{\mathbf{x}_i\}_{\text{elig.}}$, then we have made a wrong turn; we therefore remove $\mathbf{x}_{\text{prev}}$ from $\mathcal{C}$, place $\mathbf{x}_{\text{prev}}$ in the list of excluded points $\{\mathbf{x}_i\}_{\text{excl.}}$, and return to step 1 with $\mathbf{x}_{\text{prev}}$ taken from the previous iteration.

3. If $\mathbf{x}_{\text{next}}$ is a nearest neighbor of $\mathbf{x}_{\text{start}}$, and $\mathcal{C}$ contains at least ten points, then we consider the loop core closed. Otherwise, we repeat steps 1-2 until $\mathcal{C}$ is closed.

By following the path of largest $|\nabla \mathbf{n}|$ or smallest S, the loop core advances through the connected subset until it closes. In some instances steps 1-3 produce a curve that does not thread through the defect loop, but instead forms a small loop in one portion of the defect subset. In these cases we run the algorithm again with a different starting point, chosen by the next-largest $|\nabla \mathbf{n}|$ value or next-smallest S value in $\mathcal{D}$. To obtain the loop normal $\mathbf{N}$, the loop core is fit to a circle, and the normal to the plane of the circle serves as $\mathbf{N}$. An arbitrary choice of sign for $\mathbf{N}$ determines the positive sense of rotation around the loop. The local tangent vector $\mathbf{t}$ to the disclination is determined by the vector difference between next and previous points in the loop core, with sign chosen by the positive sense of rotation.

Calculating the rotation vector and reference director To calculate $\mathbf{\Omega}$ at a given point P on the loop core, we first make a collection of directors $\{\mathbf{n}(\mathbf{x}_i)\}$ from points $\{\mathbf{x}_i\}$ that are near P and nearly in the plane Θ transverse to $\mathbf{t}$. More specifically, $\{\mathbf{x}_i\}$ is the set of points with separation vector $\mathbf{d}_i$ from P satisfying $d_{\min} \leq |\mathbf{d}_i| \leq d_{\max}$ and $|\arccos(\mathbf{d}_i \cdot \mathbf{t})| > \psi_{\min}$. We use $d_{\min} = 3$, $d_{\max} = 7$, and $\psi_{\min} \approx 0.61 \times (\pi/2)$, where lengths are given in units of the voxel spacing.

Next, for each point $\mathbf{x}_i$, we project $\mathbf{d}_i$ into the transverse plane Θ, $\mathbf{d}_i^{\perp} = \mathbf{d}_i - \mathbf{t}(\mathbf{d}_i \cdot \mathbf{t})$, to obtain an angle ϕ_i in the plane relative to a fixed reference direction. The collection of directors $\{\mathbf{n}(\mathbf{x}_i)\}$ is then plotted on the unit sphere in order of ϕ_i. A semi-circle is fitted to the path traced out by this ordered collection of directors, with a definite orientation given by the positive sense of rotation in Θ, whose positive normal direction is aligned with $\mathbf{t}$. We thus compute $\mathbf{\Omega}$ as the positive normal direction to this fitted semi-circle on the unit sphere. We also take the reference director $\mathbf{n}_{\text{out}}$ to be the $\mathbf{n}(\mathbf{x}_i)$ at the point $\mathbf{x}_i$ in the collection for which $\mathbf{d}_i$ is most nearly outward from the center of the circle fitted to the loop. Any small component of this $\mathbf{n}(\mathbf{x}_i)$ along $\mathbf{\Omega}$ is projected out to obtain $\mathbf{n}_{\text{out}}$.

Calculating disclination loop topology: We measure the topological index ν of a disclination loop as follows: At roughly even intervals around a loop separated by angle $\Delta\phi$, we calculate $\mathbf{\Omega}$ and $\mathbf{n}_{\text{out}}$ to find the frame $\mathbf{F}(\phi)$ at each step. We record the $SO(3)$ rotation operation $\mathbf{R}_{\phi,\phi+\Delta\phi}$ that takes $\mathbf{F}(\phi)$ into $\mathbf{F}(\phi+\Delta\phi)$ and use $\Delta\phi$ between $2\pi/12$ and $2\pi/8$. Expressing $\mathbf{R}_{\phi,\phi+\Delta\phi}$ as a rotation by angle α about an axis $\hat{a}$, we convert the rotation to a quaternion $q_{\phi,\phi+\Delta\phi} = \cos(\alpha/2)1 - \sin(\alpha/2)(\hat{a}\cdot\vec{\sigma})$, where $\vec{\sigma} = i\hat{x}+j\hat{y}+k\hat{z}$ (borrowing from the Pauli matrix language). The product $q_{0,2\pi} = \prod_{\phi=0}^{2\pi-\Delta\phi} q_{\phi,\phi+\Delta\phi}$ identifies the loop with one of the cases named in Sec. 3, as $q_{0,2\pi}$ must be one of the following: 1 (unlinked and neutral), -1 (unlinked and charged), or a quaternion satisfying $q^2 = -1$ (linked).

5 Supplementary movie captions

Movie S1. Dynamics of a 3D active nematic, an active isotropic fluid and a passive nematic lacking ATP fuel. The left panel shows widefield fluorescent images of the microtubule bundles, while the right panel shows the birefringence obtained from polarized microscopy. Active and passive nematics exhibit birefringence that indicates local nematic order. In comparison, the 3D active isotropic fluid is not birefringent. The samples are in a thin flow chamber (100 μm thickness).

Movie S2. Z-scan of 3D active nematic cross-sections obtained with a light sheet microscope. The left panel shows the nematic director in red, overlaid onto fluorescent images of the microtubule bundles. The right panel shows the nematic director in red, overlayed onto a color map indicating the elastic distortion energy in the one constant approximation.

Movie S3. Three-dimensional structure of disclination lines. Thresholding the elastic distortion energy reveals curvlinear structure, which suggests presence of topological defects. A system spanning network of line defects is depicted in green and closed loop defects are shown in red. Sample volume is 400 μm x 400 μm x 380 μm.

Movie S4. Dynamics of disclination lines. Temporal evolution of the disclinaion lines, indicated in green. Animation focuses on an extended single line defect which breaks up, almost simultaneously emitting two loop defects. Both emitted loops quickly self-annihilate. Disclination coloring indicates β, as defined in Fig. 3.

Movie S5. Nucleation of disclination loops. Experiments: A disclination loop is created through a bend instability in a defect-free region of the nematic. Hybrid lattice Boltzmann: Formation of a pure-twist loop defect. This nucleation event is analogous to the experimentally observed nucleation of the pure-twist loop defect described in Figure 5. Finite difference: Wedge-twist loop created through a bend instability. In both simulation approaches, the white rods in the right panel indicate the director field of a plane intersecting the loop. Disclination coloring indicates β, as defined in Fig. 3.

Movie S6. Collapse and self-annihilation of disclination loops. Experiments: A wedge-twist loop closes and self-annihilates. The loop is viewed both from the side (left) and from above (right). The right panel shows a plane of the director field that intersects the loop. Hybrid lattice Boltzmann: Collapsing wedge-twist loop leaves behind an aligned director field. Finite difference: Collapse of an almost pure-twist disclination loop. In both approaches, the rods in the right panel indicate the director field of a plane intersecting the loop, while disclination coloring indicates β, as defined in Fig. 3.

Movie S7. Merging of disclinations through reconnection events. Experiments: Experimental observation of a loop defect merging with a line defect. Hybrid lattice Boltzmann: Wedge-twist loop defect shown merging with a neighboring line defect. A twist section of the loop merges with a twist section of a line. Finite difference: Loop defect merging with a line defect. In both simulation approaches, the rods in the right panel indicate the director field of a plane intersecting the loop. Disclination coloring indicates β, as defined in Fig. 3.

Movie S8. Splitting of disclinations through reconnection events. Experiments: Experimental observation of a line defect ejecting a loop defect. Hybrid lattice Boltzmann: Loop defect in simulation splitting through the reconnection of two disclination lines. The loop defect is observed to begin shrinking. Finite difference: Loop defect observed to split from a line defect. In both simulation approaches, the white rods in the right panel indicate the director field of a plane intersecting the loop. Disclination coloring indicates β, as defined in Fig. 3.

Movie S9. Structure of disclination lines. Schematic of a local $+1/2$ wedge winding character which continuously transforms into -1/2 wedge through an intermediate twist winding character. The director field winds by π about the rotation vector ω (black arrows), which makes angle β with the tangent. For $+1/2, -1/2$ wedge windings, β=0 and π respectively. $\beta = \pi/2$ indicates local twist disclination profile. Reference director $\mathbf{n}_0$ (brown) is held fixed. Rod coloring indicates the angle β, as defined in Fig. 3.

Movie S10. Nucleation of a pure-twist disclination loop. The director field is shown at three different heights, together in perspective (top) and separately in top view (bottom row). Distortion between the green plane (bottom left) and the orange plane (bottom right) causes a local twist which relaxes though the creation of a pure-twist defect loop in the purple plane (bottom center). Disclination coloring indicates the angle β, as defined in Fig. 3.

6 Supplementary figures

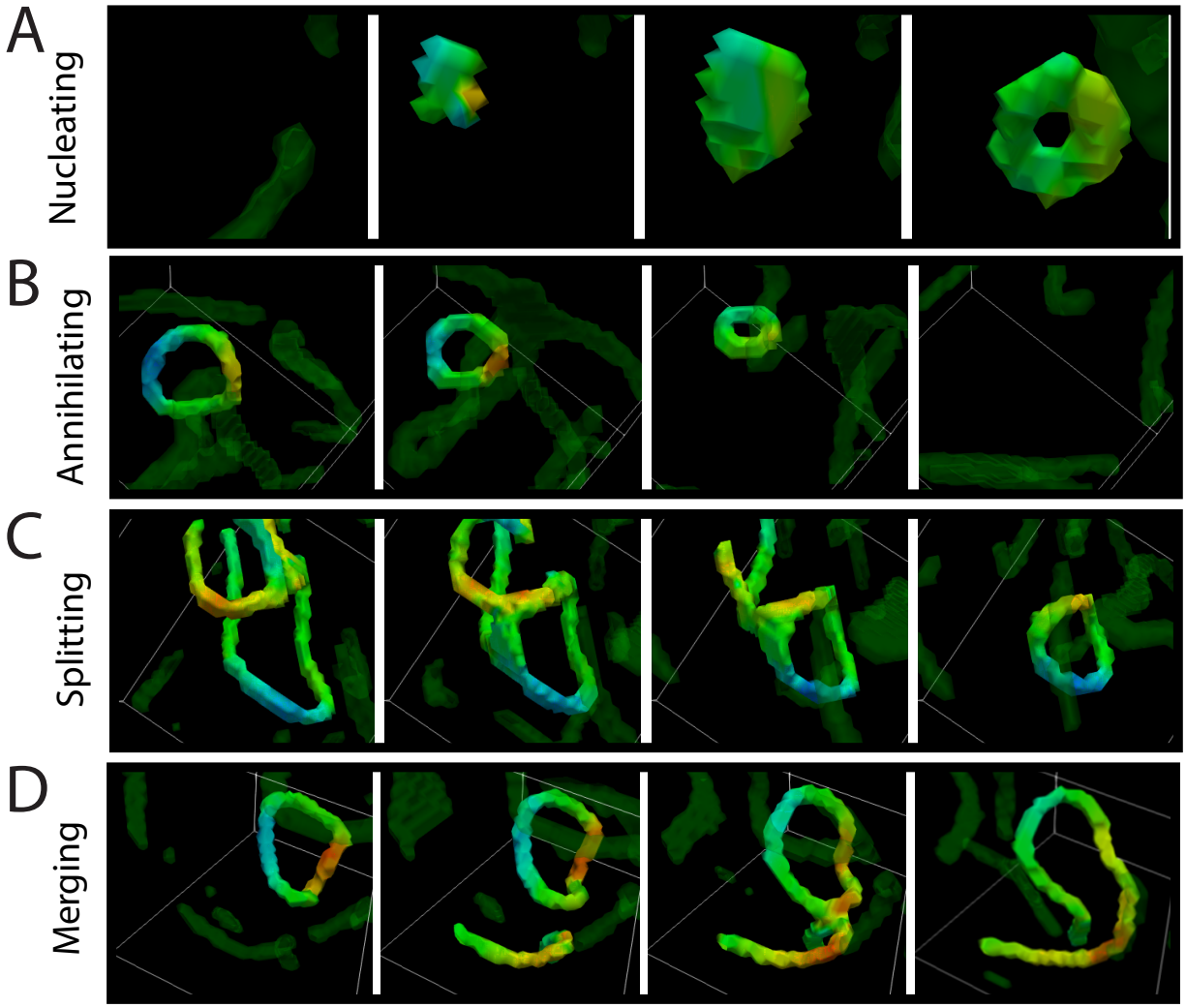

Fig. S1: Dynamics of disclination loops observed in hybrid lattice Boltzmann simulations. (A) Loop nucleation from a defect-free region. (B) Loop self-annihilation leaves behind a defect-free nematic. (C) A disclination line self-intersects and splits, emitting a loop. (D) A disclination loop merges with a disclination line. Coloring of the disclinations indicates β.

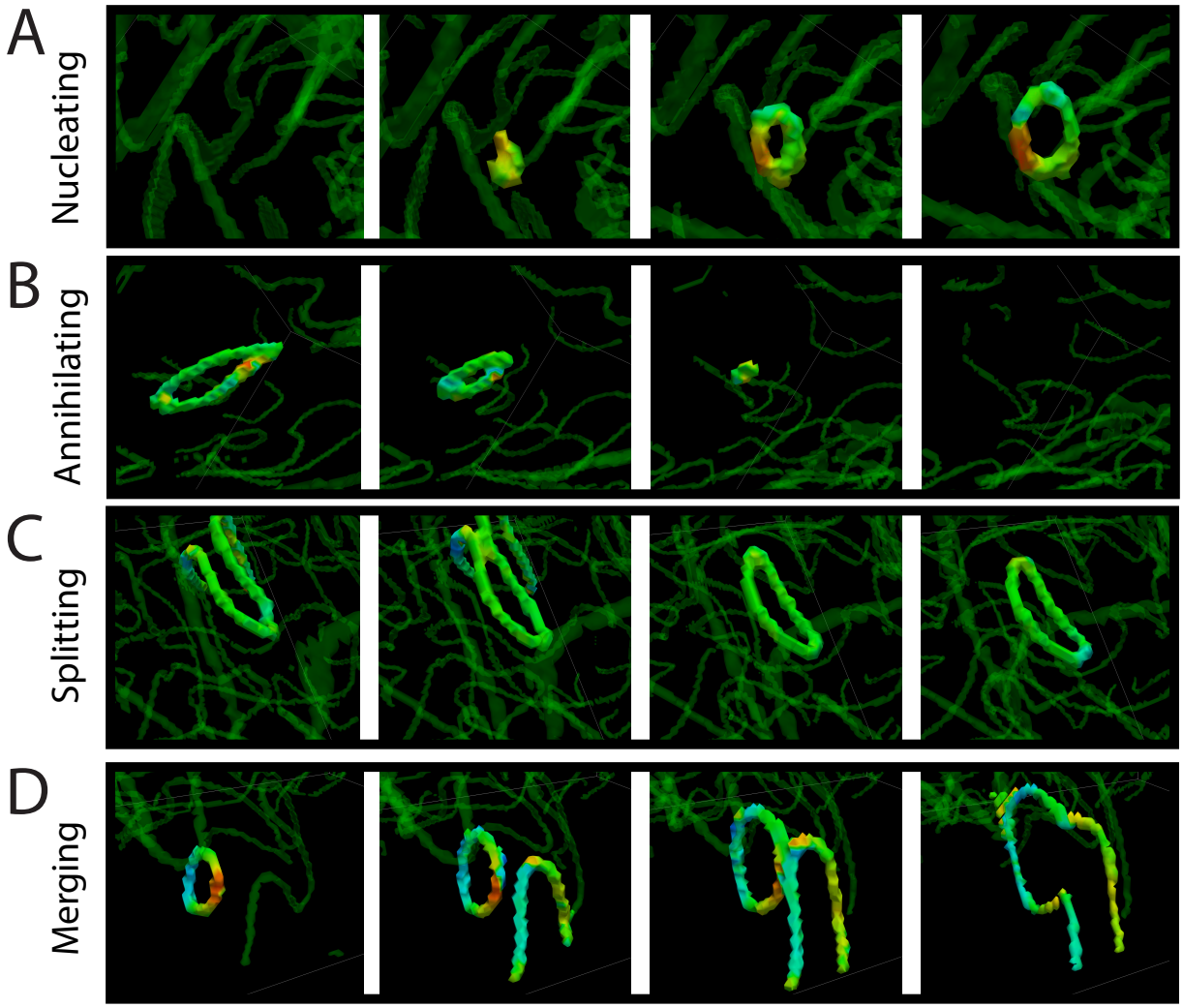

Fig. S2: Dynamics of disclination loops observed in finite difference simulations. (A) Loop nucleation from a defect-free region. (B) Loop self-annihilation leaves behind a defect-free nematic. (C) A disclination line self-intersects and splits, emitting a loop. (D) A disclination loop merges with a disclination line. Coloring of the disclinations indicates β.

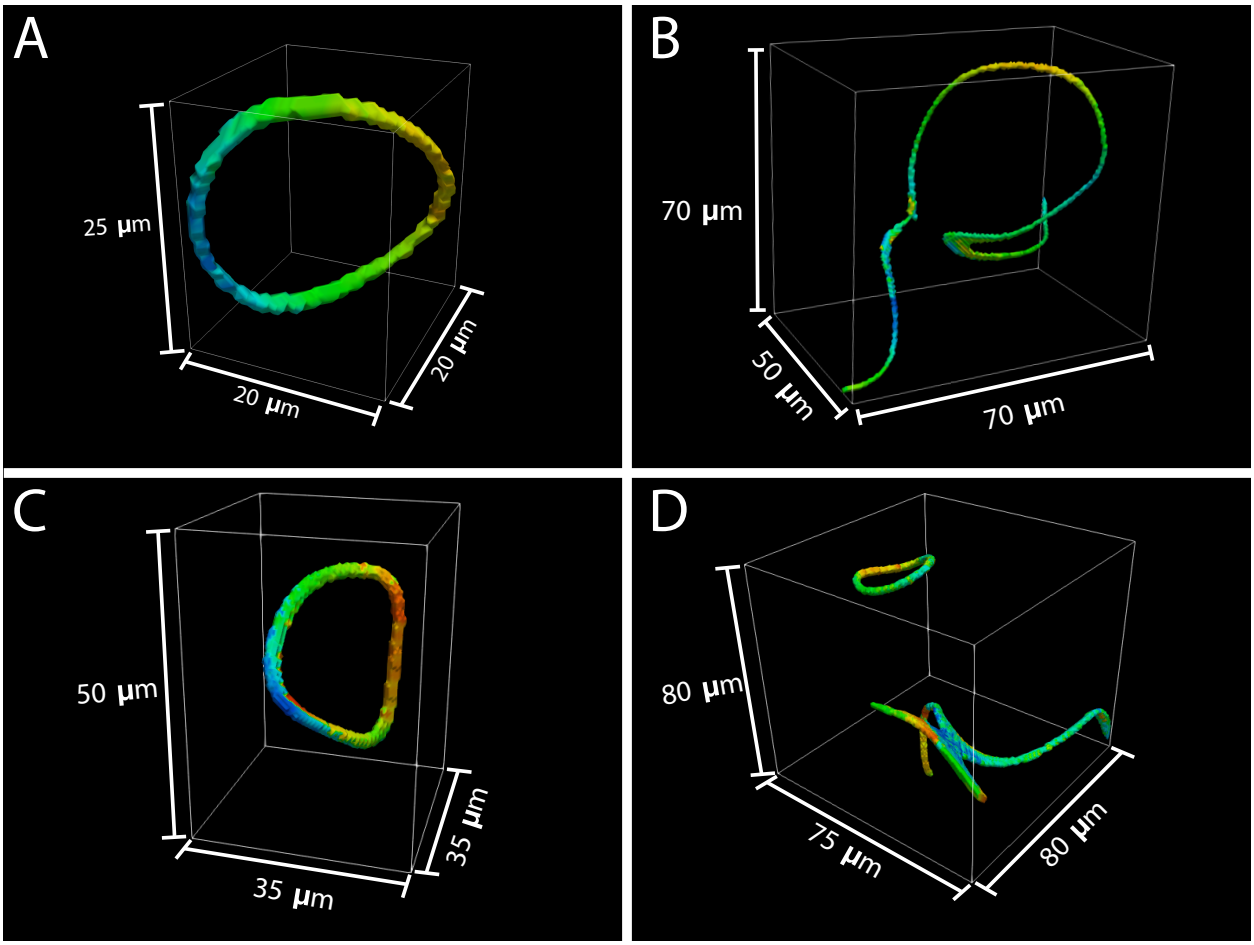

Fig. S3: Scale of the loops shown in Fig. 2. Bounding boxes are shown to give the scale of the (A) nucleation event, (B) splitting event, (C) annihilation event and (D) merging event. Coloring of the disclinations indicates β.

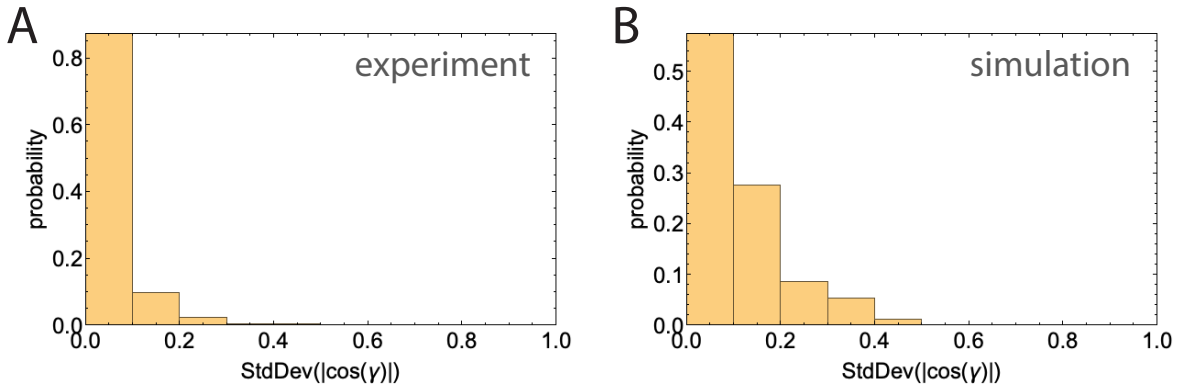

Fig. S4: Disclination loops have nearly uniform $\mathbf{\Omega}$ and $\mathbf{n_0}$ Wider distribution of $|\cos(\gamma)|$ indicate more non-uniform loops. $|\cos(\gamma)|$ is the locally calculated angle between the loop normal and $\mathbf{\Omega}$. Each standard deviation value pertains to one loop, with $\mathbf{\Omega}$ calculated at 8 to 12 approximately evenly spaced points along the loop contour. N=268 for experimental loops and N=94 for simulated loops.

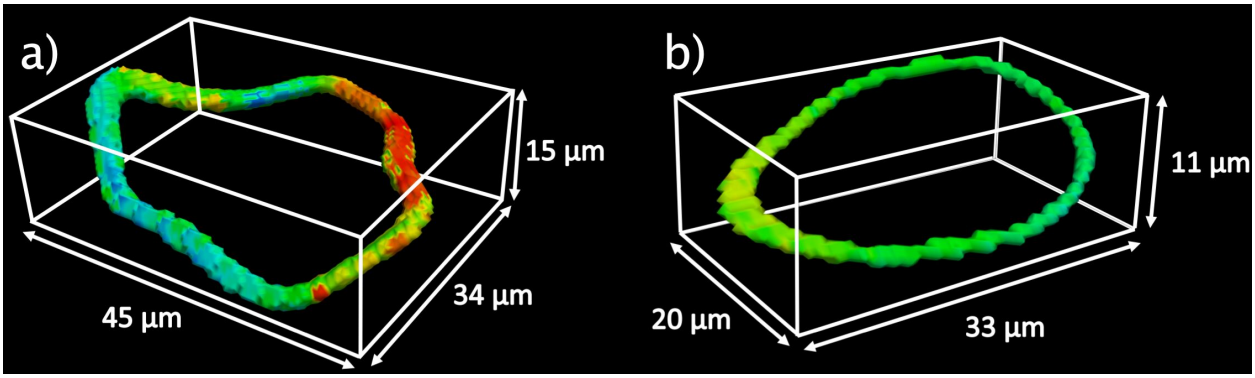

Fig. S5: Scale of the disclination loops. Bounding boxes show the scale of the experimental wedge-twist (A) and pure twist loop (B) shown in Figure 4. Disclination coloring indicates β.

References

1. M. Castoldi, A. V. Popov, *Protein Expression and Purification* **32**, 83–88, ISSN: 1046-5928 (2003).
2. A. Hyman *et al.*, in *Molecular Motors and the Cytoskeleton* (Academic Press, 1991), vol. 196, pp. 478–485.
3. S. J. DeCamp, G. S. Redner, A. Baskaran, M. F. Hagan, Z. Dogic, *Nature Materials* **14**, 1110 (2015).
4. D. S. Martin, R. Fathi, T. J. Mitchison, J. Gelles, *Proceedings of the National Academy of Sciences* **107**, 5453–5458, ISSN: 0027-8424, eprint: `https://www.pnas.org/content/107/12/5453.full.pdf`, (`https://www.pnas.org/content/107/12/5453`) (2010).
5. R. Subramanian *et al.*, *Cell* **142**, 433–443, ISSN: 0092-8674, (`http://www.sciencedirect.com/science/article/pii/S0092867410007816`) (2010).
6. P. Chandrakar *et al.*, *arXiv preprint arXiv:1811.05026* (2018).
7. T. Maniatis, J. Sambrook, E. Fritsch, *Cold Spring Harbor Laboratory Press*, 623–623 (1989).
8. E. Barry, D. Beller, Z. Dogic, *Soft Matter* **5**, 2563–2570 (2009).
9. S. J. Streichan, M. F. Lefebvre, N. Noll, E. F. Wieschaus, B. I. Shraiman, *eLife* **7**, ed. by F. Jülicher, e27454, ISSN: 2050-084X, (`https://doi.org/10.7554/eLife.27454`) (Feb. 2018).
10. J. Schindelin *et al.*, *Nature Methods* **9**, 676 (2012).
11. S. Preibisch *et al.*, *Nature Methods* **11**, 645–648 (2014).
12. R. Rezakhaniha *et al.*, *Biomechanics and Modeling in Mechanobiology* **11**, 461 (2012).
13. D. Marenduzzo, E. Orlandini, M. Cates, J. Yeomans, *Physical Review E* **76**, 031921 (2007).
14. J. Zhao, Q. Wang, *Journal of Scientific Computing* **68**, 1241–1266 (2016).
15. S. P. Vanka, *Journal of Computational Physics* **65**, 138–158 (1986).
16. M. Kleman, J. Friedel, *Reviews of Modern Physics* **80**, 61 (2008).
17. G. P. Alexander, B. G.-g. Chen, E. A. Matsumoto, R. D. Kamien, *Reviews of Modern Physics* **84**, 497 (2012).

18. K. Jänich, *Acta Applicandae Mathematica* **8**, 65–74 (1987).

19. S. Čopar, S. Žumer, *Proceedings of the Royal Society A: Mathematical, Physical and Engineering Science* **469**, 20130204 (2013).

20. L. Tran *et al.*, *Proceedings of the National Academy of Sciences* **113**, 7106–7111 (2016).

21. A. Lozano-Durán, G. Borrell, *ACM Transactions on Mathematical Software (TOMS)* **42**, 34 (2016).

22. J. Toriwaki, T. Yonekura, *Forma* **17**, 183–209 (2002).